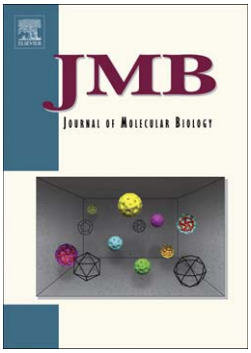

Enhanced Local Disorder in a Clinically Elusive von Willebrand Factor Provokes High-Affinity Platelet Clumping

Alexander Tischer, Venkata R. Machha, Juan P. Frontroth, Maria A. Brehm, Tobias Obser, Reinhard Schneppenheim, Leland Mayne, S. Walter Englander, Matthew Auton

PII: S0022-2836(17)30242-5
DOI: doi:10.1016/j.jmb.2017.05.013
Reference: YJMBI 65415

To appear in: *Journal of Molecular Biology*

Received date: 7 April 2017
Revised date: 10 May 2017
Accepted date: 15 May 2017

Please cite this article as: Tischer, A., Machha, V.R., Frontroth, J.P., Brehm, M.A., Obser, T., Schneppenheim, R., Mayne, L., Walter Englander, S. & Auton, M., Enhanced Local Disorder in a Clinically Elusive von Willebrand Factor Provokes High-Affinity Platelet Clumping, *Journal of Molecular Biology* (2017), doi:10.1016/j.jmb.2017.05.013

Enhanced Local Disorder in a Clinically Elusive von Willebrand Factor Provokes High-Affinity Platelet Clumping.

Alexander Tischer[1], Venkata R. Machha[1], Juan P. Frontroth[2]*, Maria A. Brehm[3], Tobias Obser[3], Reinhard Schneppenheim[3]*, Leland Mayne[4], S. Walter Englander[4]* and Matthew Auton[1]*

[1] Division of Hematology, Departments of Internal Medicine and Biochemistry and Molecular Biology, Mayo Clinic, Rochester, MN, 55905, USA

[2] Laboratorio de Hemostasia y Trombosis, Servicio de Hematologia y Oncologia, Hospital de Pediatria, "Prof. Dr. Juan P. Garrahan", Buenos Aires, Argentina.

[3] Department of Paediatric Haematology and Oncology, University Medical Centre Hamburg-Eppendorf, Hamburg, Germany.

[4] Johnson Research Foundation, Department of Biochemistry and Biophysics, Perelman School of Medicine, University of Pennsylvania, Philadelphia, PA 19104, USA

* Corresponding authors: Juan P. Frontroth, jfrontroth@garrahan.gov.ar, Reinhard Schneppenheim, schneppenheim@uke.de, Walter Englander, engl@mail.med.upenn.edu or Matthew Auton, auton.matthew@mayo.edu, phone: +01 (507) 284-3776

Running Title: Structural Resolution of High-Affinity VWF

Keywords: von Willebrand factor, von Willebrand disease, Hydrogen-Deuterium Exchange Mass Spectrometry, GPIbα.

Abbreviations Used: HXMS, Hydrogen Exchange Mass Spectrometry; SPR, surface plasmon resonance; CD, circular dichroism; VWF, von Willebrand factor; VWD, von Willebrand disease; Ristocetin, a macroglycopeptide antibiotic; DDAVP, 1-desamino-8-D-arginine vasopressin; RCAM, reduced and carboxyamidated; VWF:Ag, VWF Antigen; VWF:RCo, VWF Ristocetin cofactor activity; RIPA, ristocetin-induced platelet agglutination; VWF:CB, VWF Collagen Binding; PT, Prothrombin time; aPTT, activated partial thromboplastin time; FVIII:C, Factor VIII.

Abstract (limit 250 words): 235
Number of figures/tables: 8/2
Number of references: 54

Abstract

Mutation of the cysteines forming the disulfide loop of the platelet GPIbα adhesive A1 domain of von Willebrand factor causes quantitative VWF deficiencies in the blood and von Willebrand disease. We report two cases of transient severe thrombocytopenia induced by DDAVP-treatment. Cys1272Trp and Cys1458Tyr mutations identified by genetic sequencing implicate an abnormal gain-of-function phenotype, evidenced by thrombocytopenia, that quickly relapses back to normal platelet counts and deficient plasma VWF. Using surface plasmon resonance, analytical rheology, and hydrogen-deuterium exchange mass spectrometry (HXMS), we decipher mechanisms of A1-GPIbα mediated platelet adhesion and resolve dynamic secondary structure elements that regulate the binding pathway. Constrained by the disulfide, conformational selection between weak and tight binding states of A1 takes precedence and drives normal platelet adhesion to VWF. Less restrained through mutation, loss of the disulfide preferentially diverts binding through an induced-fit disease pathway enabling high-affinity GPIbα binding and firm platelet adhesion to a partially disordered A1 domain. HXMS reveals a dynamic asymmetry of flexible and ordered regions common to both variants indicating that the partially disordered A1 lacking the disulfide retains native-like structural dynamics. Both binding mechanisms share common structural and thermodynamic properties, but the enhanced local disorder in the disease state perpetuates high-affinity platelet agglutination, characteristic of type 2B VWD, upon DDAVP-stimulated secretion of VWF leading to transient thrombocytopenia and a subsequent deficiency of plasma VWF, characteristic of type 2A VWD.

Introduction

The primary hemostatic function of the human von Willebrand factor (VWF) is to sequester platelets from blood flow in response to vascular injury so that secondary hemostasis and blood coagulation can proceed to stop the bleeding [1]. Like a fishing line with multiple hooks, VWF is a multidomain multimeric plasma glycoprotein with multiple sites (A1 domains) to which platelets adhere. Efficient formation of a hemostatic platelet plug is dependent on the high molecular weight multimeric forms of VWF in plasma. Similar to the quantitative VWF deficiency phenotypes of von Willebrand disease (VWD), lack of the mid to high molecular weight multimers of VWF multimers in type 2A VWD significantly impairs primary hemostasis causing hemorrhage.

Type 2A VWD refers to qualitative functional variants in which VWF-dependent platelet adhesion is diminished or absent because the proportion of large VWF multimers is decreased [2]. This limits the detection of VWF in blood and its ristocetin cofactor activity in clinical assays [3]. Ristocetin is a standard macroglycopeptide antibiotic used to induce *in vitro* VWF-platelet agglutination in patient plasma in order to assess gain or loss-of-function. Subtypes of 2A result from mutations that impair intracellular multimerization [4] and mutations that enhance the degradation of high molecular weight multimers by the blood metalloprotease, ADAMTS13 [5]. A few mutations classified in the 2A phenotype, however, also occur in the platelet GPIbα binding A1 domain of VWF [6], indicating that the VWF multimer/function disproportionality characteristic of the type 2A phenotype is also a result of gain-of-function even when thrombocytopenia is not immediately apparent.

Chief among type 2A mutations are cysteine substitutions that break the disulfide bond in the A1 domain. Alkylation of these cysteines has been demonstrated to enhance GPIbα affinity and rheological platelet adhesion to recombinant A1 domains [7-10]. Recombinant VWF studies of how cysteine mutations in the A1 domain alter the ristocetin-induced platelet binding activity of VWF have been ambiguous indicating a gain or loss of function depending on which cysteine is mutated [11-12]. However, reduced and alkylated recombinant VWF shows an enhanced affinity for platelets in the absence of ristocetin [13]. Evidence for high affinity in VWD patients due to loss of the disulfide bond has not been previously observed [14-16]. Here, evidence is presented from two patients which confirms that cysteine amino acid substitutions that break the disulfide bond induce a gain-of-function phenotype that manifests in a DDAVP-

treatment-induced transient thrombocytopenia which promptly restores to a homeostasis of low VWF and normal platelet counts within hours following treatment [17,18]. DDAVP is a vasopressin analog that stimulates the release of VWF from Weibel-Palade bodies of vascular endothelial cells into the blood.

Despite two decades of research, a structure based mechanism of high-affinity binding has not been fully elucidated. The dynamic character of the A1 domain has limited many crystallographic attempts to identify a specific high-affinity conformation with type 2B gain-of-function VWD variants of the A1 domain [19-22]. Recent experimental evidence for mutation-induced A1 domain misfolding in both type 2B gain-of-function and type 2M loss-of-function VWD phenotypes has further complexed the issue [23]. These phenotypes contain many mutations that collectively enhance (2B) or diminish (2M) VWF-dependent platelet interactions, however, the extent of gain or loss-of-function is variably broad in range [23]. Here, a structural thermodynamic mechanism for high-affinity platelet adhesion to the A1 domain lacking a disulfide bond is deciphered using a combination of circular dichroism, surface plasmon resonance, analytical rheology, and hydrogen-deuterium exchange mass spectrometry (HXMS). In the normal condition, platelet GPIbα affinity is regulated by a conformational selection [24] between weak and tight binding states of A1 within the native ensemble. In disease, loss of the disulfide partially disorders the A1 domain and restricts binding through an induced-fit pathway [24] involving a conformational change from the weakly bound complex to a tightly bound complex that perpetuates abnormally high-affinity platelet adhesion. HXMS reveals that both binding mechanisms share common dynamic structural regions that regulate the thermodynamic path to high affinity. GPIbα is able to adapt to local disorder in the A1 domain through flexibility of the leucine-rich repeats and complementary disorder in a loop previously referred to as the β-switch. The interaction between platelets and VWF is driven by local flexibility within the A1 domain that, left unrestrained, leads to localized conformational disorder thereby intensifying GPIbα affinity and aggravating thrombocytopenia when patients are challenged with DDAVP.

Results and Discussion

Patients. Two unrelated girls (6.3y and 9.6y) with a historical diagnosis of type 2A VWD presented with low VWF:Ag (22 and 27%) and undetectable VWF:RCo and VWF:CB without prior evidence of thrombocytopenia or *in vitro* hyper responsiveness to low dose ristocetin

(0.5mg/mL). These presentations are typical of a type 2A diagnosis which is characterized by reduced VWF-dependent platelet adhesion due to a quantitative loss of the largest VWF multimers in plasma [16]. Desmopressin, DDAVP-treatment, is frequently used to induce release of normal VWF from cellular compartments when plasma VWF:Ag is quantitatively deficient [17], but it is contraindicated in gain-of-function type 2B VWD [25]. DDAVP-treatment of these patients induced transient thrombocytopenia in which platelet counts decreased 30 min post-DDAVP infusion from normal counts (Patient 1 = $194*10^9$ L^{-1}, Patient 2 = $274*10^9$ L^{-1}) to ($27*10^9$ L^{-1} and $52*10^9$ L^{-1}, respectively) with complete restoration at 120 min, **Fig. 1A**. Thrombocytopenia was paralleled by an increase in median platelet volume (**Table 1**) and platelet clumps were observed in blood smears, **Fig. 1B**. Spontaneous platelet aggregation and enhanced response to low dose RIPA (0.5 mg/mL) was also detected in *in vitro* plasma mixing studies at 30 min post-DDAVP infusion. Increases in VWF:CB, FVIII:C, and VWF:Ag were evident, but VWF:RCo activity remained constant and unimproved as a function of time (**Table 1**). Subsequent DNA sequencing of exon 28 of the VWF gene detected a heterozygous p.Cys1272Trp mutation in patient 1 and a p.Cys1458Tyr mutation in patient 2, both of which disrupt the disulfide bond of the VWF A1 domain, **Fig. S1**.

These observations confirm that human VWF lacking the disulfide bond of the A1 domain has high affinity for platelets and mutations at C1272 and C1458 should be classified as type 2B variants even though under a normal life, no stress or stimulated situations, patients are phenotypically 2A. DDAVP-induced thrombocytopenia has previously been observed in other noncysteine type 2B gain-of-function mutations [26], but other reported cysteine mutations [14,16] have not demonstrated gain-of-function in patients [15]. In agreement with our clinical data at "basal" times, the patient with a C1272R mutation reported by Lavergne *et al.* also had low VWF:Ag = 30 U/dl, a VWF:RCo activity < 5, and absent RIPA, but a DDAVP trial was not performed [14]. Similar results were obtained from a patient with a C1272F mutation reported by Woods *et al.* with low basal VWF:Ag = 32 U/dl, VWF:RCo/VWF:Ag ratio < 0.15 and absent RIPA at >1.5 mg/mL ristocetin [15]. A DDAVP trial previously performed on a patient with a C1272S mutation reported by Penas *et al.* in which platelet counts dropped from $200*10^9$ L^{-1} to $157*10^9$ L^{-1} at 30 min post-DDAVP treatment even though VWF:Ag, VWF:RCo, RIPA and presence of high molecular weight multimers were deficient relative to normal throughout the trial [15]. Relative to the patients reported here, DDAVP treatment of the C1272S patient only

modestly reduced the platelet count indicating that perhaps the expression of the mutation was variable as has been observed with other type 2M/2A VWD patients with the same genotype within the same family [27]. Recombinant VWF studies using ristocetin induced platelet binding have previously indicated some gain- or loss-of-function dependency on which cysteine was mutated [11] and others have demonstrated that Cys->Ala mutations can abolish RIPA [12] indicating that ristocetin based assays are not functionally effective with mutations that alter the disulfide bonding of A1 in VWF.

The transient DDAVP-induced thrombocytopenia observed here is similar to other cases of type 2B patients whose glycocalicin and P-selectin levels remained constant post-DDAVP, suggesting that type 2B VWD is hemorrhagic due to enhanced platelet agglutination rather than thrombotic as a result of platelet activation [30]. The restoration of normal platelet counts concomitant with the reduction of VWF:Ag levels and disappearance of platelet clumps (**Fig. 1B**) over time post-DDAVP indicates that the high-affinity VWF-platelet clumps eventually dissociate within the circulatory system, probably with the aid of ADAMTS13 proteolysis of VWF, until a homeostasis between platelets and deficient VWF is reattained.

Circular Dichroism Spectroscopy. To study the structural and functional consequences of the lack of a disulfide bond, Cys1272 and Cys1458 were reduced and carboxyamidated (RCAM) [10] in the normal sequence of A1. Carboxyamidation prevents undesired complications of disulfide linked dimers that would arise during expression and purification of the A1 domain with single cysteine mutations. The disulfide bond connects the C-terminus of α6-helix to the N-terminus of the β1-strand of the domain. Chemically breaking the disulfide bond induces a non-native partially disordered structure (**Fig. 2**). Circular dichroism is commonly used to determine a protein's secondary structure content and determine whether a protein has a tertiary fold. Far-UV circular dichroism (CD) shows a significant reduction in overall secondary structure content in RCAM A1 compared to the disulfide intact A1 domain resulting in an estimated loss of 13% α-helical content and gain of ~6% β-strand and ~7% random coil structure [9,10,28]. Near-UV CD of RCAM A1 shows a loss of the spectral pattern (260-300nm) relative to WT A1 indicating an absence of asymmetric chiral environments of tyrosine and tryptophan residues that are normally present in native tertiary contacts [29].

Surface Plasmon Resonance Spectroscopy. SPR was used to compare the binding kinetics and affinity of A1 and RCAM A1 to GPIbα under steady-state conditions. The real time association and dissociation of A1 or RCAM A1 and surface captured GPIbα was followed by injection of the A1 domain variants at concentrations ranging from 0.125 - 8μM A1 and 0.25 - 1μM RCAM A1. The association and dissociation phases of both A1 and RCAM A1, shown in **Fig. 3A**, are biexponential indicating the presence of two binding competent conformational states. The SPR response functions were analyzed according to a thermodynamic model (**Fig. 3B**) that accounts for an interconversion between two bound states and a dynamic equilibrium between low and high-affinity conformations within the native state of A1 and the partially disordered state of RCAM A1. Using the integrated rate equations (**Methods** and **Table 2**) that determine the flux through the thermodynamic cycles in **Fig. 3B**, two distinct modes of binding were identified.

The mechanism in the normal condition (top of **Fig. 3B**) is that A1 can dynamically adapt between weak (W) and tight (T) adhesion to GPIbα depending on the equilibrium constant, K_1 (M^{-2}), between $A1_W$ and $A1_T$ conformations. Fitting this model to the SPR response curves reveals that the association of GPIbα to either $A1_W$ or $A1_T$ will proceed at similar rates (k_3 ($M^{-2}s^{-1}$) ≈ k_4 ($M^{-2}s^{-1}$)), but dissociation from the weak $A1_WG$ complex is an order of magnitude faster than from $A1_TG$, (k_{-3} ($M^{-1}s^{-1}$) > k_{-4} ($M^{-1}s^{-1}$)). Interconversion between bound states favors the formation of the tightly bound complex by another order of magnitude, k_2 ($M^{-1}s^{-1}$) > k_{-2} ($M^{-1}s^{-1}$). The equivalence of k_3 ($M^{-2}s^{-1}$) and k_4 ($M^{-2}s^{-1}$) emphasizes that the binding is driven by a conformational selection that is determined by the conformational equilibrium in the native state which favors the weak $A1_W$ conformation. This equilibrium, $K_1 = 0.19 \pm 0.12$ (M^{-2}), corresponds to a fractional population of only ~16% $A1_T$ and ~84% $A1_W$, but this ratio is significant enough to drive the binding in both directions around the thermodynamic cycle, hence, conformational selection.

By contrast, the disorder caused by loss of the disulfide bond prevents this conformational selection and restricts the binding through a single pathway (bottom of **Fig. 3B**) resulting in an induced fit to an abnormally high-affinity complex. Even though the association and dissociation phases of RCAM A1 interaction with GPIbα remain biexponential, the equilibrium constant, $K_1 = (13.1 \pm 0.3)*10^{-7}$ (M^{-2}), strongly favors the weak conformation of RCAM A1. Paradoxically, the weak $rA1_W$ state of RCAM A1 has ~3x lower affinity ($K_3 = 1.1 \pm 0.3$ (M^{-1})) than the corresponding $A1_W$ state of the disulfide intact A1 domain, ($K_3 = 3.7 \pm 1.1$

(M^{-1})), but the association and dissociation rates are 1-2 orders of magnitude slower for RCAM A1 than for A1. The equivalence of k_3 ($M^{-2}s^{-1}$) and k_{-3} ($M^{-1}s^{-1}$) allows RCAM A1 to dynamically sample the $rA1_WG$ bound state. Once stable interactions are formed, interconversion to $rA1_TG$ is favored by an additional order of magnitude, k_2 ($M^{-1}s^{-1}$) > k_{-2} ($M^{-1}s^{-1}$). Direct dissociation from this tightly bound complex, $rA1_TG$, is highly improbable with k_4 ($M^{-2}s^{-1}$) >> k_{-4} ($M^{-1}s^{-1}$) by 7 orders of magnitude. In this disease condition, the partially disordered character of RCAM A1 enables the dynamic sampling of high-affinity contacts with GPIbα. The lower affinity and decreased rates of association and dissociation of GPIbα to and from RCAM A1 relative to A1 indicate that once the complex is formed with RCAM A1, it is more stable than the corresponding complex with A1. These observations explain why release of VWF with mutations of the A1 disulfide bond into the vasculature provokes platelet agglutination resulting in thrombocytopenia.

Analytical Rheology. The two mechanisms of conformational selection and induced fit also manifest in the shear rate dependence of platelet adhesion to the A1 domain variants under rheological flow. Rheology of platelet adhesion is experimentally quantified through instantaneous translocation velocities calculated from numerical differentiation of distance trajectories [30] and pause times; the amount of time a platelet remains stationary before the next translocation. **Fig. 4A** illustrates that the statistical mean of experimental pause time distributions is 4-5x larger for RCAM A1 than for the disulfide intact A1 at all shear rates. Likewise, the mean of experimental velocity distributions is approximately 10x slower as a function of shear for RCAM A1 than for the normal A1 domain (**Fig. 4B**). The insets of **Fig. 4A&B** compare these experimental distributions of pause time and velocity at selected shear rates spanning the full range of experimental measurements. The distributions of RCAM A1 pause times broaden to higher times than for A1 while the A1 velocity distributions broaden to higher velocities than for RCAM A1. The observation that pause time and translocation velocity mirror each other; *i.e.* greater velocities give lesser pause times and vice versa, is valid at all shear rates investigated. A comparison of platelet translocations on A1 and RCAM A1 at a physiological shear rate of $1500s^{-1}$ in **Movies S1&S2** illustrate that RCAM A1 can support platelet clumping in addition to stable platelet adhesion, therefore, supporting the histology observations of the patients (**Fig.1B**).

Integral analysis of the pause time distributions yields biexponential decay survival fractions (inset of **Fig. 4C)** that quantify the rates of dissociation of platelets from the A1 domain as a function of the rheological shear rate. Analysis of these survival fractions (**Methods**), gives apparent rate constants for the dissociation from two bound states, k_{-3} (s^{-1}) and k_{-4} (s^{-1}) (**Fig. 4C**), and interconversion between bound state conformations, k_2 (s^{-1}) and k_{-2} (s^{-1}) (**Fig. 4D**). As expected, the dissociation rates, k_{-3} (s^{-1}) and k_{-4} (s^{-1}), increase with increasing rheological shear, indicating that shear stress favors the dissociation of both bound conformations although k_{-3} (s^{-1}) is faster than k_{-4} (s^{-1}). This rheological increase in the rates of dissociation for both A1 and RCAM A1 causes the diminishing pause times and enhanced translocation velocities as the rheological shear increases. Shear, however, affects the equilibrium between bound conformations differently for A1 than for RCAM A1 (inset of **Fig. 4D**). In the A1 domain, k_2 (s^{-1}), the rate of conversion to the high-affinity $A1_TG$ complex is constant as the shear increases, but the reverse rate, k_{-2} (s^{-1}), increases with shear and shifts the equilibrium back in favor of the weak $A1_WG$ complex. At the highest shear rate measured for A1 ($9000s^{-1}$), the equilibrium constant, $K_2 \approx 1$, and both $A1_WG$ and $A1_TG$ are equally probable. By contrast, k_2 (s^{-1}) for RCAM A1 always exceeds k_{-2} (s^{-1}) and the equilibrium ($K_2 > 1$) between bound conformations remains constant and always in favor of the tightly bound complex, $A1_TG$. Taken together, these results indicate that when the disulfide bond is present, increasing shear stress can shift the equilibrium in favor of the weakly bound conformation and facilitate dissociation of platelets from VWF. Loss of the disulfide bond abolishes this regulatory mechanism.

Hydrogen-deuterium eXchange Mass Spectrometry. Hydrogen-deuterium exchange experiments identify local regions of protein flexibility by exploiting the principle that the amide backbone unit of every amino acid (except proline) can dynamically swap a hydrogen atom with solvent deuterium atoms present in a solution of D_2O. This process is often dynamically controlled by local conformational fluctuations of secondary structures within proteins. Hydrogen-deuterium exchange of A1 and RCAM A1 was measured as a function of time to identify the structural determinants that give rise to high affinity. **Fig. 5** illustrates a kinetic time dependence of exchange within various secondary structure regions of the A1 domain over a 24 hr period. Although hydrogen exchange throughout the domain is slow, the data demonstrate that exchange occurs in localized regions that are common to both A1 and RCAM A1. **Fig. 6**

illustrates two of these HX time points (10s and 60min) of exchangeable regions within A1 and RCAM A1 as a function of residue number (**Fig. 6A**) mapped onto the crystal structure of the A1 domain (**Fig. 6B**). Enhanced exchange within RCAM is observed primarily in the α2 and the following loop connecting α3, the 3_{10}-helix prior to α4, and parts of β2, β4 and α5. HX of the N-terminal peptide region prior to C1272 of A1 and RCAM A1 is identical for both proteins within experimental error (**Fig. 5**). In contrast, the β2-β3 hairpin and the α3 helix remain as protected from exchange in RCAM A1 as they are in A1 (**Fig. 5**) indicating that these structures remain hydrogen-bonded despite the increased disorder of the flanking helices in RCAM A1. Exchange in the central β4 strand of the β-sheet after 60min incubation indicates that loss of the disulfide bond significantly perturbs the hydrophobic core of the A1 domain as expected from the molten globule character observed by circular dichroism (**Fig. 2**) [10]. Both variants, however, share the same dynamic structural regions indicating that, even in the partially disordered state, RCAM A1 retains some of the native-like structural properties of the disulfide-intact A1. These identified structural regions are likely responsible for the thermodynamic regulation of the strength of platelet adhesion to VWF. Restraining the conformational dynamics of these structural regions through disulfide bonding enables the conformational selection that drives normal platelet adhesion, but less restrained in this disease condition, they are free to sample abnormal high-affinity contacts with GPIbα leading to extraordinarily high-strength bonds with platelets through an induced fit mechanism.

It is important to recognize the significance of localized structural flexibility. Prior experimental and computational evidence supports these HXMS observations that structural dynamics and localized disorder drives high affinity between A1 domain and GPIbα. All atom MD simulations and thermodynamic algorithms predict localized dynamics and thermodynamic asymmetry of the domain [32,33] particularly within the α2-loop-α3 sequence. It is probable that mutations can alter the binding path within the constraints of the thermodynamic cycle presented in **Fig 3B**. For example, type 2B gain-of-function mutations in and around the α2 helix thermodynamically and kinetically destabilize the native state forcing the conformational selection, K_1, in favor of $A1_T$ (a shift in equilibrium) or misfold the A1 domain so that the thermodynamic flux is shunted through the induced fit pathway through $A1_W$ [9,24,31]. Conversely, a type 2M loss-of-function G1324S mutation in the β2-β3 hairpin stabilizes the A1 domain by constraining the conformational flexibility of the domain so that A1 becomes

kinetically trapped in the $A1_W$ state [34]. Enhanced dynamics caused by type 2M VWD mutations in stable secondary structure elements, like the α3 helix, misfold A1 and abolish platelet adhesive function [23] potentially leading to completely off-pathway conformational states. The HXMS results support the body of thermodynamic and mutational evidence that certain secondary structures must remain ordered (such as the β2-β3 hairpin and the α3 helix) to maintain binding competency while disorder in other flanking regions (such as α2 and the 3_{10}-helix) enable the dynamic regulation of the strength of VWF-platelet bonds.

GPIbα also plays a dynamic role in the interaction. **Fig. 7** illustrates that hydrogen exchange is localized to the β-switch (residues Y228-A244) and the convex surface of the leucine-rich repeats (LRRs). In contrast, HX within the concave β-sheet is minimal, even after 20hrs of exchange, indicating that these parallel β-strands make up a stable hydrogen-bonded network. The dynamics of GPIbα are analogous to a hand, where the concave β-sheet represents the palm of the hand, the convex LRR surface represents the dorsum (top) of the hand, and the β-switch loop is like a disordered opposable thumb. Viewed in this manner, the localized dynamics would allow flexible bending of the LRR region enabling GPIbα to grasp the A1 domain of VWF while the disorder in the thumb dynamically samples the A1 domain for high-affinity contacts. This type of behavior is compatible with the experimental thermodynamic mechanisms presented in **Fig. 3B** in that GPIbα searches for an induced fit to the A1 domain to enable high-affinity adhesion while the LRR can flex around the A1 domain to enhance electrostatic contacts. Recent cocrystal structures of A1 containing gain-of-function VWD mutations in complex with GPIbα containing gain-of-function platelet-type VWD mutations show a gained interaction specifically between K1371 in the loop following the α3-helix of the A1 domain and various polar and acidic GPIbα residues in LRR's 3-4 [22]. When the disulfide is intact, this search by GPIbα is frustrated by the A1 equilibrium constant, K_1, that drives conformational selection. When the disulfide is broken, GPIbα is free to search ($K_3 \approx 1$) for high-affinity contacts with disordered regions of RCAM A1 and accommodate an induced fit enabling a firm grasp of VWF.

Analysis of crystal structures of GPIbα with platelet-type VWD mutations that increase affinity reveal a potential disruption of conformational preferences for the opposable thumb to favor a 3_{10} helix structure or a conserved D_{235}-K_{237} salt bridge thereby enabling stretching to the extended conformation found in cocrystal complexes with A1 [35], but crystal structures can often be deceiving [36]. GPIbα preferentially interacts with the disordered RCAM A1

conformational state with high-affinity. Gain-of-function PT-VWD mutations, G233V, M239V and D235Y [37,38], increase the opposable thumb's hydrophobicity from a grand average hydropathy of -0.006 to 0.265, 0.129 and 0.124, respectively [39]. The search for high-affinity contacts by GPIbα's disordered opposable thumb suggests that increased hydrophobicity of the thumb might allow for a greater sampling of dynamically exposed hydrophobic regions of A1 enabling the formation of hydrophobic contacts that stabilize the complex through an induced fit. The most hydrophobic helix (0.214) of A1, α3, is a probable candidate structure since it remains ordered and protected from exchange in both disulfide-intact and RCAM A1. Alternatively, and perhaps more likely, platelet-type VWD mutations in this opposable thumb may kinetically destabilize GPIbα leading to an enhanced affinity as has been observed for type 2B VWD mutations (R1306Q and I1309V) in the natively folded conformation of the A1 domain [23,34].

In contrast to proposed mechanisms that require a disorder to β conformational switch in GPIbα's opposable thumb for binding to occur [40-42], hence the name β-switch, the structural thermodynamics perspective is that the interaction between platelets and VWF is driven by dynamic local disorder. **Fig. 8A** compares HX of the free and GPIbα-bound states of A1 and RCAM A1 at 1hr of hydrogen exchange and illustrates that HX is decreased in the complex throughout the entire sequence. Mapped to the crystal structure of A1 in **Fig. 8B&C**, all exchanged regions of the free A1 and RCAM A1 (left) become protected in the bound state (middle) so that the Delta (Free-Bound, right) mirrors the structural dynamics of the free state of RCAM A1. Therefore, all exchanging structural regions of each variant participate in a high-affinity complex with GPIbα. Furthermore, the bound states are identical in their HX, within error, indicating that both A1 and RCAM A1 bound to GPIbα obtain similar high affinity conformations. This key observation supports the thermodynamics in **Fig. 3B** in that both conformational selection and induced fit binding mechanisms share common bound states. Breaking the disulfide bond likely releases conformational strain in the α6-helix [43], which loosens the entire structure enabling it to conformationally adapt to its GPIbα receptor without disrupting the overall conformation of the binding interface.

Thermodynamic cycles involving two binding competent conformational states have been considered before with limitations. The use of equilibrium binding models coupled with atomic force microscopy and thermodynamics of partial denaturation by urea was approximate, but over-estimated the energetics of conformational change within the native state ensemble [9].

Single molecule force spectroscopy used in conjunction with thermodynamic models gives apparent on and off rates as a function of force, but the thermodynamic linkage through the equilibrium, K_1, between free states was not explicitly considered [44,45]. The force-induced rate switching observed by Kim *et. al.* could result from conformational selection due to thermodynamic linkage, but could also result from microscopic irreversibility in favor of the higher affinity state of A1 in the single-molecule construct [45], a complication that is not shared by analytical rheology.

Conclusions

The DDAVP-induced transient thrombocytopenia and the platelet clumping histology observed with these patients confirms a stimulated release of high-affinity VWF lacking the A1 disulfide bond as a result of p.C1272W and p.C1458Y mutations. Although prior recombinant studies of VWF and single A1 domains have demonstrated a high affinity when the disulfide is broken [7-13], direct evidence patients has not been realized. Furthermore, the biophysical studies performed here put fine mechanistic and structural detail to the interaction that has not been previously elucidated. It is possible, however, that the amino acid specific substitutions may leave the free cysteine available for abnormal disulfide pairing with other domains in VWF or make additional thermodynamic contributions that reduction and carboxyamidation of the cysteines does not capture [11].

SPR and analytical rheology quantify the thermodynamic flux at equilibrium and the unbinding flux as a function of shear stress enabling a mechanistic interpretation of how VWD mutations and rheology alter the binding path. This provides a framework that enables the prediction of additional altered binding modes that could lead to gain-of-function as well as loss-of-function. For example, an equilibrium shift of K_1 in favor of $A1_T$ would also lead to a 2B phenotype and a kinetic trap in favor of $A1_W$ would similarly result in a type 2M phenotype.

HXMS provides the added near-residue-resolved structural insight and identifies secondary structure elements which participate in the binding regardless of whether A1 remains natively structured or partially disordered. As such, HXMS also has the capability to decipher local disorder induced by disease mutations in both gain- and loss-of-function VWD. With the current methods in place, a structure-resolved mechanistic phenotyping of VWD becomes a real

possibility that when combined with genotyping enables the prediction of how VWD patients manifest the symptoms of disease.

Materials and Methods

Patients. The clinical management and the laboratory patient studies were performed in the Laboratory of Thrombosis and Hemostasis of the Hospital de Pediatria "Prof. Dr. Juan P. Garrahan". DDAVP (1-desamino-8-D-arginine vasopressin) was infused intravenously (0.3 µg/kg body weight in 50ml of normal saline) over a period of 30 minutes. Blood samples were obtained before infusion and 30, 60, 120 and 240 min after starting DDAVP infusion. Platelet count was performed by an electronic counter (Sysmex XS-800i, Sysmex Corporation, Kobe, Japan). Morphology of blood smears was evaluated with a Nikon Eclipse E200 microscope (Nikon, Tokyo, Japan). Prothrombin time (PT), activated partial thromboplastin time (aPTT) and factor VIII (FVIII:C) were assessed by standard methods by means of an automated coagulometer (STA Compact, Diagnostica Stago, Asnieres, France). VWF:RCo was determined by aggregometry using normal formalin-fixed platelets (FFP) and a final concentration of ristocetin of 1.0 mg/mL (Biopool, Trinity Biotech PLC, Bray, Ireland). The final mix assayed was 400 µl of FFP and 50 µl of plasma plus 50µl Ristocetin 10mg/ml. Aggregometry was performed on a dual-channel Chrono-Log Lumi-Aggregometer (Chrono-Log Corporation, PA, USA). Calibration curve for VWF:RCo was made from a local normal-plasma-pool comprising 352 individuals used as a secondary standard calibrated against standard #02/150 of the National Institute of Biological Standards and Control (NIBSC). VWF:Ag was determined by latex-immunosorbent-assay (LIA). VWF:CB was determined by an in-house ELISA method. See **Table 1** for these clinical labs post-DDAVP infusion. Sequencing of exon 28 was performed using PCR amplification product and BigDye Terminator version 3.1 cycle sequencing kit (Applied Biosystems) on an automated ABI PRISM 3130 capillary sequencer (Applied Biosystems), **Fig. S1**.

Protein expression, purification and quantification. A1 (amino acids Q1238 - P1471) was expressed as inclusion bodies in *E. coli* as fusion construct containing an N-terminal 6xHis-Tag in the pQE9 plasmid. GPIbα (amino acids M1 - E301) was expressed in cell culture in HEK293

cells as a fusion construct containing a C-terminal 6xHis-Tag and a C-terminal FLAG-Tag in the PIRES neo 2 plasmid.

The A1 inclusion body preparation, refolding and purification via Ni^{2+}-NTA and Heparin Sepharose affinity chromatography was performed as recently described [23,46]. GPIbα was purified via the 6xHis-Tag. RCAM A1 was generated in 2M GdnHCl by reducing the single disulfide bond of A1 with 6mM DTT followed by addition of 12mM Iodoacetamide as previously described [3]. Protein concentrations were determined spectrophotometrically using extinction coefficients at 280nm of 15350 L/mol/cm for A1/RCAM A1 and 33900 L/mol/cm for GPIbα as calculated from the number of tyrosine and tryptophans in the amino acid sequence.

Circular Dichroism spectroscopy. CD spectra were recorded on an Aviv Biomedical Model 420SF circular dichroism spectrometer. Far UV CD Spectra of A1 and RCAM A1 were measured between 190 - 260nm in a 0.1mm quartz cell at 20°C. Spectra in the near UV range were recorded at room temperature between 260 - 360nm using a 10cm cylindrical quartz cell. The step width for all CD spectra was 1nm, the integration time 60s. All spectra were corrected for the signal of the corresponding buffer and converted to mean ellipticity per amino acid residue (Θ^{MRW}).

Surface Plasmon Resonance. Kinetics of A1 and RCAM A1 binding to GPIbα were obtained using a BIACORE T-100. Amine coupling kit, CM5 biochip and HBS-EP+ buffer were purchased from BIACORE. Anti-FLAGTag M2 antibody was purchased from Sigma-Aldrich. Anti-FLAGTag M2 antibody for capturing FLAG-tagged GPIbα was diluted into 10 mM sodium acetate (pH 4.5) to 50µg/ml concentration and immobilized covalently on the active (Fc2) and the reference (Fc1) channel of the CM5 chip using the amine coupling kit reagents (EDC (1-ethyl-3-[3-dimethylaminopropyl]carbodiimide), NHS (N-hydroxysuccinimide) and ethanolamine). ~8000 RU of immobilization levels were obtained on both channels. Real time binding between A1 or RCAM A1 (concentration ranging from 0.125µM to 8µM) and anti-FLAG captured GPIbα were measured at 25°C in kinetics mode using TBS buffer (pH 7.4) at a flow rate of 30µL/min. Each binding cycle started by loading 2µM GPIbα at a flow rate of 30µl/min for 400s, followed by a 100s buffer wash step. A1 or RCAM A1 was injected in a 200s association phase followed by injection of buffer in a 100s dissociation phase. Each analyte

concentration was injected twice for reproducibility. Between each binding cycle, the anti-FLAG surface was regenerated with an injection of 10mM glycine at pH 2.0 for 60s. The signal of the blank (buffer) was subtracted from all kinetic responses before analysis to remove non-specific interactions and to reduce baseline drifts from dissociating GPIbα. Analysis of the SPR response functions was performed as described in the Supporting Information.

Analytical Rheology. Parallel plate flow chamber studies were performed as previously described [10, 47] on a Zeiss Axio Observer A1 microscope using a PCO edge camera at 25 frames per second. Citrated whole blood obtained by informed consent according to Mayo Institutional Review Board approval was perfused at a shear rate of $800s^{-1}$ over 5μM A1/RCAM A1, that was immobilized prior to the measurement via the N-terminal 6xHis-Tag. After the removal of red blood cells, the shear rate was increased in logarithmic intervals to a maximum of $9000s^{-1}$ for A1 and $70000s^{-1}$ for RCAM A1. For each shear rate, movies of platelets translocating on the flow chamber surface were recorded for 60s. Distance trajectories were calculated from platelet coordinates and numerically differentiated to obtain instantaneous velocities as a function of time [30]. Pause times were determined by the amount of time a platelet was not moving in consecutive frames. Mean pause times and velocities were calculated from statistical distributions of pause time and instantaneous velocity events.

Pause time distributions for each shear rate were converted to pause time survival fractions using the following equation.

$$\frac{\#PT_{total} - \sum_{t=0}^{t} \#PT_t}{\#PT_{total}}$$

where $\#PT_{total}$ is the total number of pause time events and $\#PT_t$ is the total number of pause time events that are less than or equal to time, t. The SPR dissociation equations, given in the Supporting Information, were fit to experimental survival fractions at each shear rate with the fractional constraint that $C_1 + C_2 = 1$ at zero pause time. To validate the thermodynamic model for platelet adhesion, mean lifetimes $\langle \tau \rangle$ were calculated from the experimentally determined rate constants obtained from fitting the above dissociation equations to the pause time survival fractions using the following equation [48]:

$$\langle \tau \rangle = -\int_{t=0}^{\infty} t \cdot \frac{d([A1_W G](t) + [A1_T G](t))}{dt} \cdot dt$$

Validation was confirmed by agreement between the lifetimes calculated from the thermodynamic model and the mean of pause times distributions determined from the experimental platelet trajectories. Furthermore, the shear rate dependence of the rate constants was well described by power functions, $k(\gamma) = a\,\gamma^b$. Substitution of these power functions for each rate constant into the above equation gives the mean lifetime $\langle \tau \rangle$ (γ) as a function of shear rate, which also agreed with the experimental pause time data.

Hydrogen/Deuterium Exchange Mass Spectrometry. A detailed scheme of the experimental setup is shown in **Fig. S3** as described by Mayne *et. al.* [49,50]. HX protein samples were prepared by adding 100µL of protein solution (in TBS or PBS, pH 7.4) to 400 µL TBS in D_2O (pD 7.4) resulting in 80% v/v D_2O. The samples were mixed and after various times (10s to overnight incubation) the reaction was quenched by a drop in pH to 2.7 via addition of 5µL HCl to the solution. Target pH values were determined prior to the HX experiment. The quenched samples were mixed again and injected manually into a 200µL loop within the cooling box. The manual injection port was coupled with the Orbitrap mass spectrometer to send a start impulse that triggered the experiment with a 5min data acquisition delay. The injected protein was loaded on a pepsin column (custom packed, bed volume 80 or 400µL) using 0.1% formic acid at pH 2.7 at an isocratic flow rate of 200µL/min. Proteolytic peptides were collected on a C8 trap column and after 5min a second valve was used to switch the trap column from isocratic flow to a water/acetonitrile gradient (20µL/min, 1-40% Acetonitrile in 18min, followed by a steep gradient to 90% in 2min). The gradient elutes peptides from the trap column which are subsequently separated by a reverse phase C18 column prior to the electrospray emitter of the LTQ Orbitrap XL for mass determination. All columns and the whole flow system are kept within a Peltier cooled chamber at ~ 0 °C to minimize back exchange of the deuterium during pepsinolysis and peptide separation.

The orbitrap mass spectrometer was operated at a resolution of 60000 with normal mass range and positive polarity. The data were collected in profile mode. The spray voltage of the

ESI source was set to 3.5kV, the capillary voltage was 33V, the tube lens voltage was 245V and the capillary temperature was set to 150°C. MS/MS CID fragment ions were detected using the ion trap analyzer of the spectrometer in centroid mode using normal mass range and scan rate. The collision induced dissociation energy was at 35% for 20ms at a Q=0.25. In each scan the four most intense peptide ions were selected for MS/MS analysis using four additional dependent scan events.

To study the HD exchange of RCAM A1 bound to immobilized GPIbα, a second HPLC system (Beckman System Gold, pump model 126, UV detector 166) was installed next to our HXMS setup. A detailed scheme of the modified experimental setup is shown in **Fig. S4**. RCAM A1 was loaded into a 1mL loop and injected onto a 3.2mL GPIbα column at a flow rate of 1mL/min using PBS as mobile phase. Protein that did not interact with GPIbα was observed by UV absorption at 280nm. After 6min the programmable solvent switch of the Beckman HPLC pump was set to flow TBS in D_2O over the column. This flow was maintained for a variable amount of time (5min, 1h or 6h), followed by switching the solvent to 0.1% formic acid, pH 2.7 to quench the HD exchange reaction. The flow rate was reduced to 0.5mL/min to prevent overpressure and as soon as an increase in absorbance was observed, indicating that the solution is sufficiently acidic to prevent inactivation of the pepsin column and that RCAM A1 starts to elute from the column, a manual solvent switch before the UV detector was triggered and the flow was diverted to the pepsin column and the HXMS flow system. After ~5min, the Orbitrap experiment was started and after another 5min the C8 trap column was switched in-line with the Water/Acetonitrile gradient as described above.

Peptide map, HD exchange and data analysis. To yield an all-H sample that was used for peptide retention time calibration and for obtaining a peptide map, A1 and GPIbα (all in TBS or PBS, pH 7.4) were acidified to a final pH of 2.7 and injected onto the pepsin column. Proteolytic peptides were collected on a C8 trap column and separated afterwards by a C18 column followed by injection into the mass spectrometer as described above. To identify A1 and GPIbα peptides, a Sequest search within Bioworks 3.3.1 (Thermo Fisher Scientific) was used to analyze the obtained MS/MS data. The search was performed using a large database of proteins that also contained several decoy proteins and reversed sequences to ensure the correctness of the

identified A1/RCAM A1 and GPIbα peptides. The search tolerance for the peptides was set to 4ppm and the fragment ion tolerance was 0.1amu.

Successfully identified peptides were used to generate exclusion lists for additional all-H experiments to increase the number of found peptides by deselecting previously identified peptides. The software EXMS 2 [51], developed by the Englander lab, was used to generate a peptide map and the resulting site resolution index for A1 and RCAM A1 using a P_{Pep} cutoff of 0.99.

Deuterated peptides of A1, RCAM A1 and GPIbα were identified using EXMS2 with the previously generated peptide map and the first all-H run. The m/z tolerance was 10ppm, the retention time window for the the all-H sample was 4min and for the deuterated sample 1min. The individual peak noise threshold was set to 500 and the summed peak noise threshold was at 1500.

The multi-threaded HD-site analysis [52] for all samples was performed on a Dual Xeon W5590 server equipped with 96GB of memory. The HD-site analysis was performed using an experimental temperature of 25°C and a pD = 7.4. Since we are unable to obtain an all D sample of our proteins, no back exchange correction was performed. The fitting level was set to Envelope and the fitting algorithm used was LsqNonLin. The range of the deuteration was 0 to 0.8. After the analysis, switchable peptides were averaged manually.

Preparation of Pepsin and GPIbα columns. Porcine pepsin was purchased from Promega and coupled to Poros AL20 column matrix using a Schiff´s base chemistry as described by Wang [53]. 100mg of Pepsin was dissolved in 2mL of 50mM NaCitrate pH 4.4. The coupling reaction was performed on ice in a 10mL beaker under slow stirring. To the pepsin solution 0.33mL of 1M $NaCNBH_4$ (Sigma Aldrich) was added followed by slow addition of 1.5M Na_2SO_4. Then 0.7g of Poros AL20 powder was added to form a homogenous suspension. 2.3mL of Na_2SO_4 were added drop by drop over a period of 2h. The suspension was then transferred into a 15mL tube and incubated at 4°C for 18h under gentle mixing.

The reaction was quenched by addition of 100µL 1M Ethanolamine solution and incubated further under gentle mixing for 4-5h at 4°C. Free pepsin was removed from the preparation afterwards by washing the column matrix with 50 mM NaCitrate, pH 4.4. The

column matrix was then packed into small HPLC columns (bed volumes ranging from 80-800μL) and the pepsin columns were cleaned excessively with 0.1% formic acid at pH 2.7.

Prior to the coupling of GPIbα to the Poros AL20 matrix we ensured that the protein would not denature in 0.1% formic acid. Therefore we measured a CD spectrum of the protein in PBS at pH 7.4 followed by a drop in pH to 2.7. A kinetic measurement and a spectrum both showed no significant difference. The coupling of GPIbα to the PorosAL20 matrix was identical to the procedure used for pepsin but was performed in PBS instead of the Citrate buffer. The GPIbα matrix was packed into a column with a total bed volume of 3.2mL.

Acknowledgments

This work was supported by National Institutes of Health Grant HL109109 from NHLBI (to M.A.), GM031847 from NIGMS (to S.W.E.), and the Great Lakes Hemophilia Foundation and the Health Resources and Services Administration through the Mayo Clinic Comprehensive Hemophilia Treatment Center (to M.A.). We also gratefully acknowledge charitable contributions to Mark Davies' Cycle Von Willebrand Disease which have defrayed, in part, publication costs.

Author Contributions

JPF managed the VWD patients. MAB, TO and RS provided the GPIbα. AT and VRM expressed and purified proteins. VRM performed the SPR experiments. MA derived and performed the SPR and analytical rheology analysis. AT, MA and VRM performed and analyzed analytical rheology experiments. AT, MA, and LM performed the HXMS experiments. MA, AT, LM and SWE designed the HXMS studies. MA, AT, VRM and JPF wrote the paper.

Conflicts of Interest

None.

References

1. Springer T.A. (2014) von Willebrand factor: Jedi knight of the bloodstream. Blood. 124(9):1412-1425.

2. Nichols W.L., Hultin M.B., James A.H., Manco-Johnson M.J., Montgomery R.R., Ortel T.L., Rick M.E, Sadler J.E. & Yawn B.P. (2008). von Willebrand disease (VWD): evidence-based diagnosis and management guidelines, the National Heart, Lung, and Blood Institute (NHLBI) Expert Panel report (USA). Haemophilia, 14(2):171-232.

3. Roberts J.C. & Flood V.H. (2015) Laboratory diagnosis of von Willebrand disease. Int J Lab Hematol. 37 (Suppl. 1):11-17.

4. Schneppenheim R., Budde U. & Ruggeri Z. (2001) A molecular approach to the classification of von Willebrand disease. Best Pract Res Clin Haematol. 14(2):281-298

5. Zheng X.L. (2013) Structure–function and regulation of ADAMTS-13 protease. J Thromb Haemost. 11 (Suppl. 1):11-23.

6. Von Willebrand Factor Variant Database, a member of the"European Association for Haemophilia and Allied Disorders" Coagulation Factor Variant Databases. The University of Sheffield. https://grenada.lumc.nl/LOVD2/VWF/home.php?select_db=VWF.

7. Miyata S., Goto S., Federici A.B., Ware J. & Ruggeri Z.M. (1996) Conformational changes in the A1 domain of von Willebrand factor modulating the interaction with platelet glycoprotein Ibalpha. J Biol Chem. 271:9046-9053.

8. Miyata S. & Ruggeri Z.M. (1999) Distinct structural attributes regulating von Willebrand factor A1 domain interaction with platelet glycoprotein Ibalpha under flow. J Biol Chem. 274:6586-6593.

9. Auton M., Zhu C. and Cruz M.A. (2010) The Mechanism of VWF-Mediated Platelet GPIbα Binding. Biophys J. 99(4):1192-1201.

10. Tischer A., Madde P., Blancas-Mejia L.M. and Auton M. (2014) A molten globule intermediate of the von Willebrand factor A1 domain firmly tethers platelets under shear flow. Proteins. 82:867-878.

11. Siguret V, Ribba AS, Christophe O, Cherel G, Obert B, Rouault C, Nishikubo T, Meyer D, Girma JP, and Pietu G. (1996) Characterization of recombinant von Willebrand factors mutated on cysteine 509 or 695. Thromb Haemost 76:453-459.

12. Azuma H, Hayashi T, Dent JA, Ruggeri ZM, Ware J. (1993) Disulfide bond requirements for assembly of the platelet glycoprotein Ib-binding domain of von Willebrand factor. J Biol Chem 268:2821-2827.

13. Sugimoto M., Dent J., McClintock R., Ware J. and Ruggeri Z.M. (1993) Analysis of Structure-Function Relationships in the Platelet Membrane Glycoprotein Ib-binding Domain of von Willebrand's Factor by Expression of Deletion Mutants. J Biol Chem. 268(16):12185-12192.

14. Lavergne J.M, De Paillette L., Bahnak B.R. Ribba A.S., Fressinaud E. Meyer D. & Peitu G. (1992) Defects in type IIA von Willebrand disease: a cysteine 509 to arginine substitution in the mature von Willebrand factor disrupts a disulphide loop involved in the interaction with platelet glycoprotein Ib-IX. Br J Haematol. 82:66-72.

15. Penas, N., Perez, A., Gonzalez-Boullosa, R. & Batlle, J. (2004). C1272S: a new candidate mutation in type 2A von Willebrand disease that disrupts the disulfide loop responsible for the interaction of VWF with platelet GP Ib-IX. Am J Hematol. 75(2):73-77.

16. Woods A.I., Sanchez-Luceros A., Kempfer A.C., Powazniak Y., Calderazzo Pereyra J.C., Blanco A.N., Meschengieser S.S. & Lazzari M.A. (2012) C1272F: a novel type 2A von Willebrand's disease mutation in A1 domain; its clinical significance. Haemophilia. 18:112–116.

17. Federici A.B. (2008) The use of desmopressin in von Willebrand disease: the experience of the first 30 years (1977–2007). Haemophilia. 14 (Suppl. 1):5-14.

18. Frontroth J.P., Pepe C.M, Hepner M.D., Sciuccati G., Pieroni G., Annetta S.E. & Cervio C. (2015). Thrombocytopenia during DDAVP test in two children with type 2A von Willebrand Disease. PO644-MON, ISTH 2015 Congress Meeting, Toronto, Canada.

19. Celikel, R., Ruggeri, Z. M. & Varughese, K.I. (2000). von Willebrand factor conformation and adhesive function is modulated by an internalized water molecule. Nat Struct Biol. 7(10):881-884.

20. Huizinga E.G., Tsuji S., Romijn R.A., Schiphorst M.E., de Groot P.G., Sixma J.J., & Gros P. (2002). Structures of glycoprotein Ibα and its complex with von Willebrand factor A1 domain. Science. 297(5584):1176-1179.

21. Dumas, J.J., Kumar, R., McDonagh, T., Sullivan, F., Stahl, M. L., Somers, W. S. & Mosyak, L. (2004). Crystal structure of the wild-type von Willebrand factor A1-glycoprotein Ibα complex reveals conformation differences with a complex bearing von Willebrand disease mutations. J Biol Chem. 279(22):23327-23334.

22. Blenner, M.A., Dong, X. & Springer, T.A. (2014). Structural basis of regulation of von Willebrand factor binding to glycoprotein Ib. J Biol Chem. 289(9):5565-5579.

23. Tischer A., Madde P., Moon-Tasson L. and Auton M. (2014) Misfolding of VWF to Pathologically Disordered Conformations Impacts the Severity of von Willebrand Disease. Biophys J. 107(5):1185-1195.
24. Hammes G.G., Chang Y-C., and Oas T.G. (2009) Conformational selection or induced fit: A flux description of reaction mechanism. Proc Nat Acad Sci USA. 106(33):13737-13741.
25. Holmberg L., Nilsson I.M., Borge L., Gunnarsson M. & Sjorin, E. (1983). Platelet aggregation induced by 1-desamino-8-D-arginine vasopressin (DDAVP) in Type IIB von Willebrand's disease. N Engl J Med. 309(14):816-821.
26. Casonato A., Steffan A., Pontara E., Zucchetto A., Rossi C., De Marco L. & Girolami A. (1999) Post-DDAVP Thrombocytopenia in Type 2B von Willebrand Disease Is not Associated with Platelet Consumption: Failure to Demonstrate Glycocalicin Increase or Platelet Activation. Thromb Haemost. 81:224-228.
27. Chen J., Hinckley J.D., Haberichter S., Jacobi P., Montgomery R., Flood V.H., Wong R., Interlandi G., Chung D.W., Lopez J.A., and Di Paola J. (2015) Variable content of von Willebrand factor mutant monomer drives the phenotypic variability in a family with von Willebrand disease. Blood. 126(2):262-269.
28. Bohm G., Muhr R. & Jaenicke R. (1992) Quantitative analysis of protein far UV circular dichroism spectra by neural networks. Prot Eng. 5(3):191-195.
29. Kelly S.M. & Price N.C. (2000) The Use of Circular Dichroism in the Investigation of Protein Structure and Function. Cur Prot Pept Sci. 1:349-384.
30. Savitzky A. and Golay M.J.E. (1964) Smoothing and Differentiation of Data by Simplified Least Squares Procedures. Anal Chem. 36(8):1627-1639.
31. Auton M., Sedlak E., Wu T., Zhu C. and Cruz M.A. (2009) Changes in Thermodynamic Stability of von Willebrand Factor Differentially Affect the Force-Dependent Binding to Platelet GPIbα. Biophys J. 97(2):618-627.
32. Liu, G., Fang, Y. & Wu, J. (2013). A mechanism for localized dynamics-driven affinity regulation of the binding of von Willebrand factor to platelet glycoprotein Ibα. J Biol Chem. 288(37):26658-26667.
33. Zimmermann M.T., Tischer A., Whitten S.T. and Auton M. (2015) Structural Origins of Misfolding Propensity in the Platelet Adhesive von Willebrand Factor A1 Domain. Biophys J. 109(2):398-406.

34. Tischer A., Campbell J.C., Machha V.R., Moon-Tasson L., Benson L.M., Sankaran B., Kim C. and Auton M. (2016) Mutational Constraints on Local Unfolding Inhibit the Rheological Adaptation of von Willebrand Factor. J Biol Chem. 291(8):3848-3859.

35. Othman M., Kaur H. and Emsley J. (2013) Platelet-type von Willebrand disease: new insights into the molecular pathophysiology of a unique platelet defect. Semin Thromb Hemost. 39(6):663-673.

36. Porter L.L. and Rose G.D. (2012) A thermodynamic definition of protein domains. Proc Nat Acad Sci U.S.A. 109(24):9420-9425.

37. Othman M., Lopez J.A., Ware J. (2011) Platelet-type von Willebrand disease update: the disease, the molecule and the animal model. Expert Rev Hematol. 4(5):475-477.

38. Enayat S., Ravanbod S., Rassoulzadegan M., Jazebi M., Tarighat S., Ala F., Emsley J. & Othman M. (2012) A novel D235Y mutation in the GP1BA gene enhances platelet interaction with von Willebrand factor in an Iranian family with platelet-type von Willebrand disease. Thromb Haemost. 108:946-954.

39. Kyte J. & Doolittle R.F. (1982) A Simple Method for Displaying the Hydropathic Character of a Protein. J Mol Biol. 157:105-132.

40. Lou J. & Zhu C. (2008) Flow induces loop-to-β-hairpin transition on the β-switch of platelet glycoprotein Ibα. Proc Natl Acad Sci USA. 105(37):4648-4653.

41. Zou X., Liu Y., Chen Z. Cardenas-Jiron G.I. & Schulten K. (2010) Flow-Induced β-Hairpin Folding of the Glycoprotein Iba β-Switch. Biophys J. 99:1182-1191.

42. Han M., Xu J., Ren Y. & Li J. (2015) Simulations of flow induced structural transition of the β-switch region of glycoprotein Ibα. Biophys Chem. 209:9-20.

43. Auton M., Sowa K., Smith S.M., Sedlak E., Vijayan V. & Cruz M.A. (2010) Destabilization of the A1 Domain in von Willebrand Factor Dissociates the A1A2A3 Tri-domain and Provokes Spontaneous Binding to Glycoprotein Ib and Platelet Activation under Shear Stress. J Biol Chem. 285(30):22831-22839.

44. Kim J., Zhang C.Z., Zhang X. & Springer T.A. (2010). A mechanically stabilized receptor-ligand flex-bond important in the vasculature. Nature. 466(7309):992-995.

45. Kim, J., Hudson, N.E. & Springer, T.A. (2015). Force-induced on-rate switching and modulation by mutations in gain-of-function von Willebrand diseases. Proc Natl Acad Sci USA. 112(15):4648-4653.

46. Campbell J., Tischer A., Machha V.R., Moon-Tasson L., Sankaran B., Kim C. & Auton M. (2016) Data on the purification and crystallization of the loss-of-function von Willebrand disease variant (p.Gly1324Ser) of the von Willebrand factor A1 domain. Data in Brief. 7:1700-1706.
47. Tischer A., Cruz M.A. & Auton M. (2013) The linker between the D3 and A1 domains of vWF suppresses A1-GPIbα catch bonds by site-specific binding to the A1 domain. Prot Sci. 22:1049-1059.
48. Thomas W.E., Forero M., Yakovenko O., Nilsson L., Vicini P., Sokurenko E. & Vogel V. (2006) Catch-Bond Model Derived from Allostery Explains Force-Activated Bacterial Adhesion. Biophys J. 90:753-764.
49. Mayne L., Kan Z-Y, Chetty P.S., Ricciuti A., Walters B.T. & Englander S.W. (2011) Many Overlapping Peptides for Protein Hydrogen Exchange Experiments by the Fragment Separation-Mass Spectrometry Method. J Am Soc Mass Spectrom. 22(11):1898-1905
50. Mayne L. (2016) Hydrogen exchange mass spectrometry. Methods Enzymol. 566:335-356.
51. Kan Z-Y, Mayne L., Chetty P.S., Englander S.W. (2011) ExMS: Data Analysis for HX-MS Experiments. J Am Soc Mass Spectrom. 22:1906-1915.
52. Kan Z-Y, Walters B.T., Mayne L., and Englander S.W. (2013) Protein hydrogen exchange at residue resolution by proteolytic fragmentation mass spectrometry analysis. Proc Nat Acad Sci USA. 110(41):16438-16443.
53. Wang L., Pan H. & Smith D.L. (2002) Hydrogen Exchange-Mass Spectrometry: Optimization of Digestion Conditions. Mol Cell Proteom. 1.2:132-138.

Tables

Table 1: Patient Clinical Lab Data.

Time post-DDAVP (min)	Basal	30	60	120	240
Patient 1, p.Cys1272Trp, c.3816C⟶G, 6.3 yrs.					
Platelets (*10^9/L)	194	27*	74*	185	177
Mean Platelet Volume (fL)	11.6	13.2	13.1	11.1	11
VWF:Ag (\%)	24	66	97	79	59
FVIII:C (\%)	23	53	52	47	35
VWF:CB (\%)	<5	11	10	7	<5
VWF:RCo (\%)	<5	<5	<5	<5	<5
aPTT (sec)	47.6	38.1	36.9	37.3	43.8
PT (\%)	94	93	89	93	92
Patient 2, p.Cys1458Tyr, c.4373G⟶A, 9.6 yrs.					
Platelets (*10^9/L)	274	52*	35	239	253
Mean Platelet Volume (fL)	10	12.7	10.1	9.6	9.5
VWF:Ag (\%)	24	45	62	53	40
FVIII:C (\%)	34	181	85	64	44
VWF:CB (\%)	<5	22	9	<5	<5
VWF:RCo (\%)	<5	<5	<5	<5	<5
aPTT (sec)	51.6	43.7	43.3	46.6	50.4
PT (\%)	72	68	67	68	69

Values of <5 are below the limit of detection. * Thrombocytopenia.

Table 2: SPR association & dissociation rate constants and equilibrium binding constants.

Constant	Native A1	RCAM A1
$K_1 = (k_2\ k_3\ k_{-4})/(k_{-2}\ k_{-3}\ k_4)$	0.19 ± 0.12	$(13.1 \pm 0.3)*10^{-7}$
$k_2\ (M^{-1}s^{-1})$	$(6.3 \pm 1.4)*10^{-2}$	$(2.9 \pm 0.3)*10^{-2}$
$k_{-2}\ (M^{-1}s^{-1})$	$(1.7 \pm 0.2)*10^{-2}$	$(3.9 \pm 0.5)*10^{-3}$
$K_2 = k_2/k_{-2}$	3.8 ± 1.0	7.6 ± 1.1
$k_3\ (M^{-2}s^{-1})$	1.4 ± 0.3	$(1.9 \pm 0.4)*10^{-2}$
$k_{-3}\ (M^{-1}s^{-1})$	0.38 ± 0.05	$(1.67 \pm 0.05)*10^{-2}$
$K_3 = k_3/k_{-3}\ (M^{-1})$	3.7 ± 1.1	1.1 ± 0.3
$k_4\ (M^{-2}s^{-1})$	1.32 ± 0.43	$(97.4 \pm 0.6)*10^{3}$
$k_{-4}\ (M^{-1}s^{-1})$	$(1.6 \pm 0.3)*10^{-2}$	$(1.51 \pm 0.02)*10^{-3}$
$K_4 = k_4/k_{-4}\ (M^{-1})$	85 ± 32	$(65 \pm 6)*10^{6}$

Figure Legends

Figure 1: A) Transient thrombocytopenia 30 min post DDAVP infusion with restoration to normal platelet counts at 120min. Inset: % VWF:Ag post DDAVP infusion. B) Platelet clumping observed in blood smears post DDAVP infusion in Patient 1 with pCys1272Trp mutation (left) and Patient 2 with pCys1458Tyr mutation (right). Magnification = 100x.

Figure 2: Far- and near-UV (*inset*) circular dichroism spectral comparison of WT A1 (closed symbols) and RCAM A1 (open symbols) indicating partial loss of secondary and tertiary structure in RCAM A1.

Figure 3: A) SPR comparison of A1 (top) and RCAM A1 (bottom) binding to M2 anti-FLAGTag captured GPIbα. B) Thermodynamic mechanisms of A1 (top) and RCAM A1 (bottom) binding to GPIbα. The comparison deciphers two distinct mechanisms in which normal binding is driven by a dynamic conformational selection between low and high-affinity conformations of the native state ensemble that regulates the balance between weak (W) and tight (T) adhesion. By contrast, the high-affinity disease condition prevents this selection and binding becomes tighter by induced fit. $A1_W$ and $A1_T$ represent weak and tight binding conformations of native A1. G $A1_W$ and G $A1_T$ represent weakly and tightly bound states of the A1 GPIbα complex. $rA1_W$ and $rA1_T$ represent weak and tight binding conformations of RCAM A1. G $rA1_W$ and G $rA1_T$ represent weakly and tightly bound states of the RCAM A1 GPIbα complex. G represents free GPIbα. K_1 is the equilibrium between weak and tight binding conformations; k_2 and k_{-2} are rates of interconversion between GPIbα bound states; k_3 and k_{-3} are the rates of association and dissociation of GPIbα to and from the weak conformations of A1 and RCAM A1; and k_4 and k_{-4} are the rates of association and dissociation of GPIbα to and from the tight binding conformations of A1 and RCAM A1.

Figure 4: Platelet adhesion to A1 and RCAM A1 under shear flow. A) Pause times determined from the mean (circles) of experimental pause time distributions (inset) and calculated (squares) from the rate constants derived from the thermodynamic model in panels C & D. Shear rate functional dependence of the pause times (lines) are calculated from the shear rate dependence of the rate constants in panels C & D. B) Translocation velocities obtained from the mean (circles)

of instantaneous velocity distributions (inset) as a function of the shear rate. C) Dissociation rate constants from low and high-affinity conformations obtained from survival fraction biexponential decay plots (inset). D) Rates of interconversion between low and high-affinity bound conformations and the shear rate dependence of the equilibrium between bound conformations. Insets of panels A, B and C illustrate the pause time and velocity distributions and pause time survival fraction of A1 and RCAM A1 at a shear rate of $9000s^{-1}$. The inset of D shows the equilibrium constant ($K_2 = k_2/k_{-2}$) for interconversion between bound conformations. k_2 and k_{-2} are rates of interconversion between GPIbα bound states; k_{-3} is the rate of dissociation of GPIbα from the weak conformations of A1 and RCAM A1; and k_{-4} is the rate dissociation of GPIbα from the tight binding conformations of A1 and RCAM A1. Comparative movies of platelet adhesion to A1 and RCAM A1 at low shear ($1500s^{-1}$) can be found in the Supporting Information.

Figure 5: Hydrogen-Deuterium exchange kinetics for A1 (closed symbols) and RCAM A1 (open symbols) of selected residues and peptide regions of secondary structure elements illustrated in **Fig. 6**. Data are average of triplicate measurements at each time point.

Figure 6: Hydrogen-Deuterium exchange of WT A1 and RCAM A1 free in solution. A) Fraction ^2H incorporated into A1 and RCAM A1 as a function of residue number at 10s and 60min exchange. Blue areas = A1; Red areas = RCAM A1. N-Terminus, α and β secondary structures, and the disulfide bond are indicated at the top. B) Exchangeable regions of WT A1 (left) and RCAM A1 (right) after a 10s (top) and 60min (bottom) exchange are projected on the crystal structure of the WT A1 domain (PDB ID 1auq). Colors and line thickness indicate: Blue/thin line - low exchange (<10% ^2H), White/medium lines - medium exchange (~25% ^2H), red/thick lines - highly exchanged (>50% ^2H), black thin lines - unresolved. Note that the structure of RCAM A1 is not native.

Figure 7: Hydrogen-Deuterium exchange of GPIbα free in solution. Fraction ^2H incorporated into GPIbα as a function of residue number at 20.5hrs (top). α and β secondary structures, glycosylation positions and disulfide bonds are indicated at the top. Exchange kinetics for GPIbα of selected residues and peptide regions of secondary structure elements ranging from 1min to

20.5hrs. Exchangeable regions are projected onto the GPIbα structure (PDB ID 1gwb). Note the considerable exchange in the β-switch loop region indicating that structural region is disordered (red area) and the convex surface of the leucine-rich repeats. Colors and line thickness indicate: Blue/thin line - low exchange (<10% ^{2}H), White/medium lines - medium exchange (~25% ^{2}H), red/thick lines - highly exchanged (>50% ^{2}H), black thin lines - unresolved.

Figure 8: Hydrogen-Deuterium exchange of A1 and RCAM A1 bound to GPIbα. A) Fraction ^{2}H as a function of residue number at 1 hr exchange. Red areas = free A1 (top) and RCAM A1 (bottom); Blue areas = GPIbα bound A1 and RCAM A1. N-Terminus, α and β secondary structures, and the disulfide bond are indicated along the top. B & C) Exchangeable regions in the free state (left), bound state (middle) and the difference (right) are mapped to the A1 domain structure (PDB ID 1auq). Colors and line thickness indicate: Blue/thin line - low exchange (<10% ^{2}H), White/medium lines - medium exchange (~25% ^{2}H), red/thick lines - highly exchanged (>50% ^{2}H), black thin lines - unresolved.

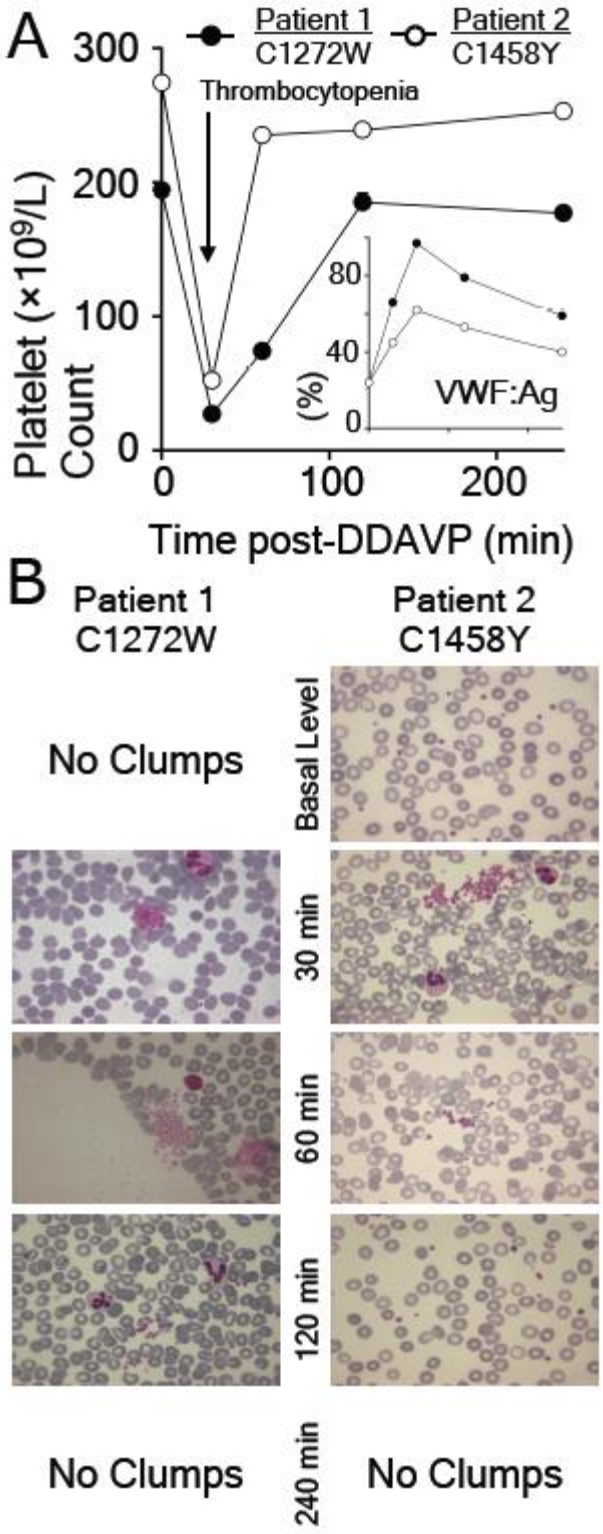

Figure 1

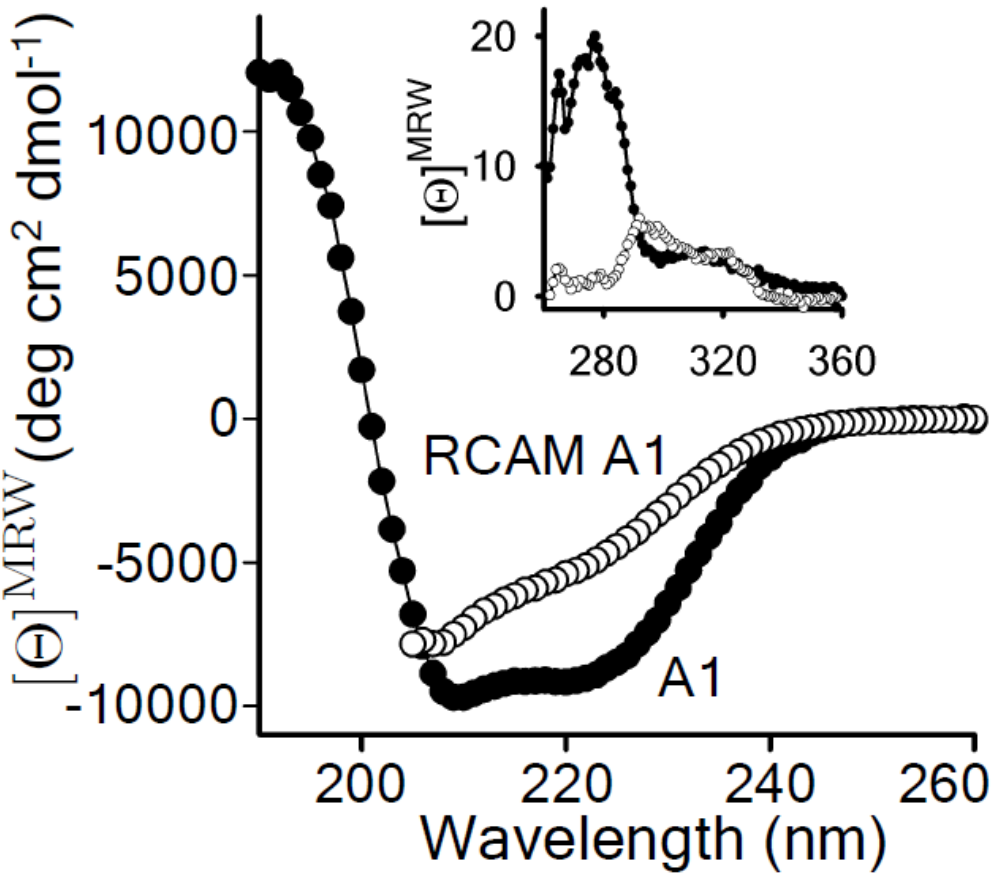

Figure 2

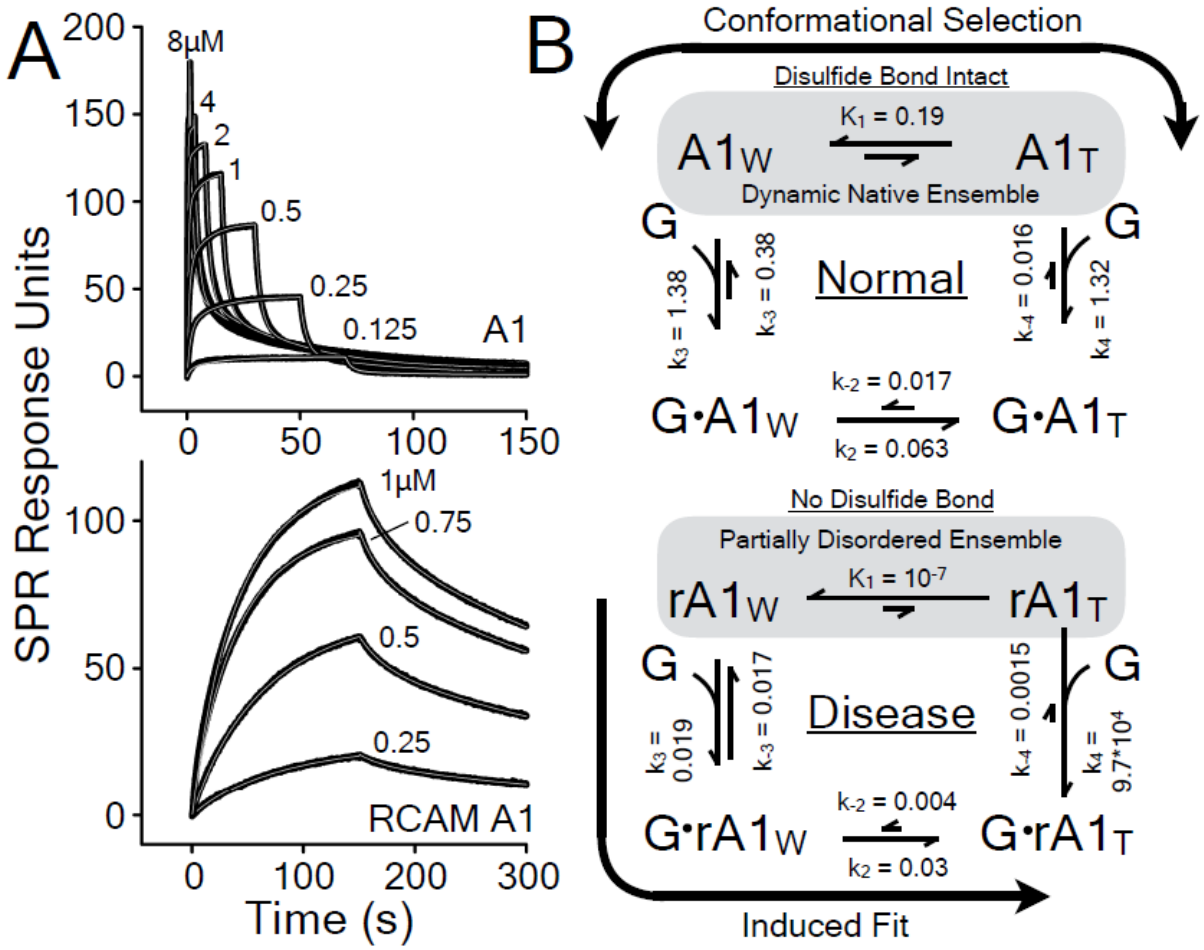

Figure 3

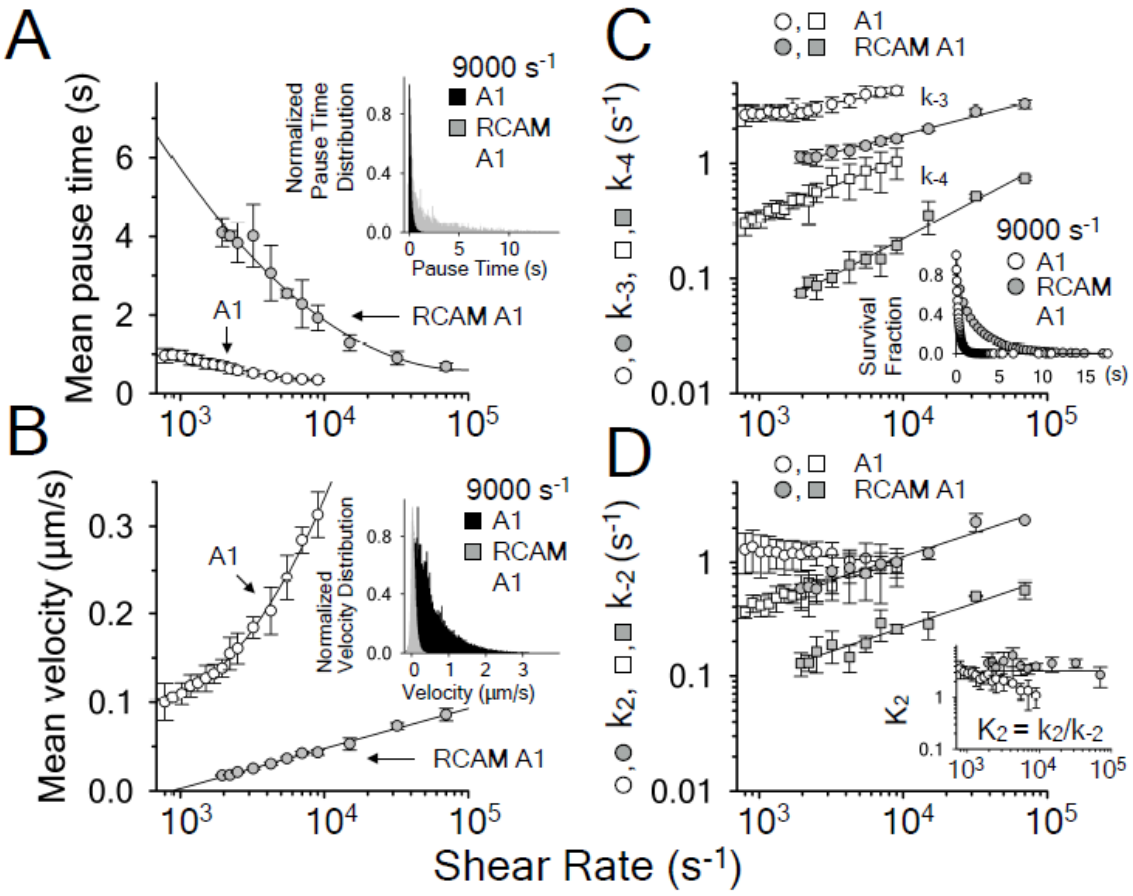

Figure 4

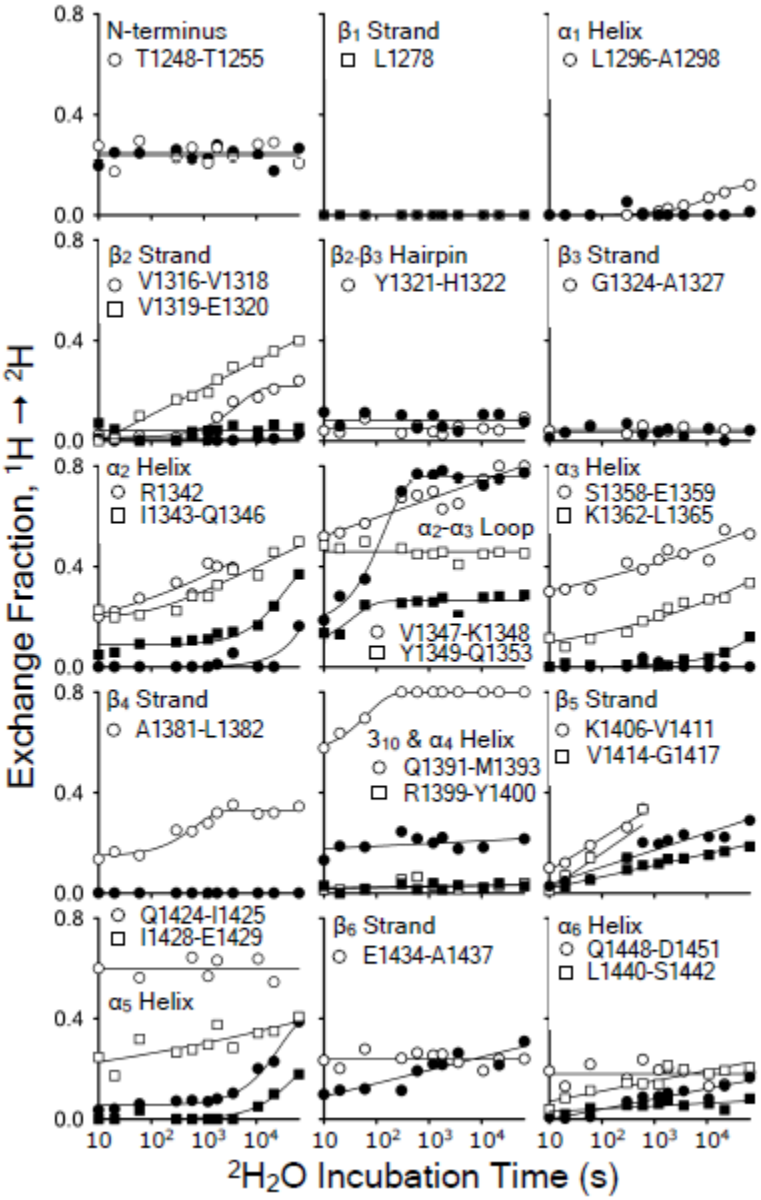

Figure 5

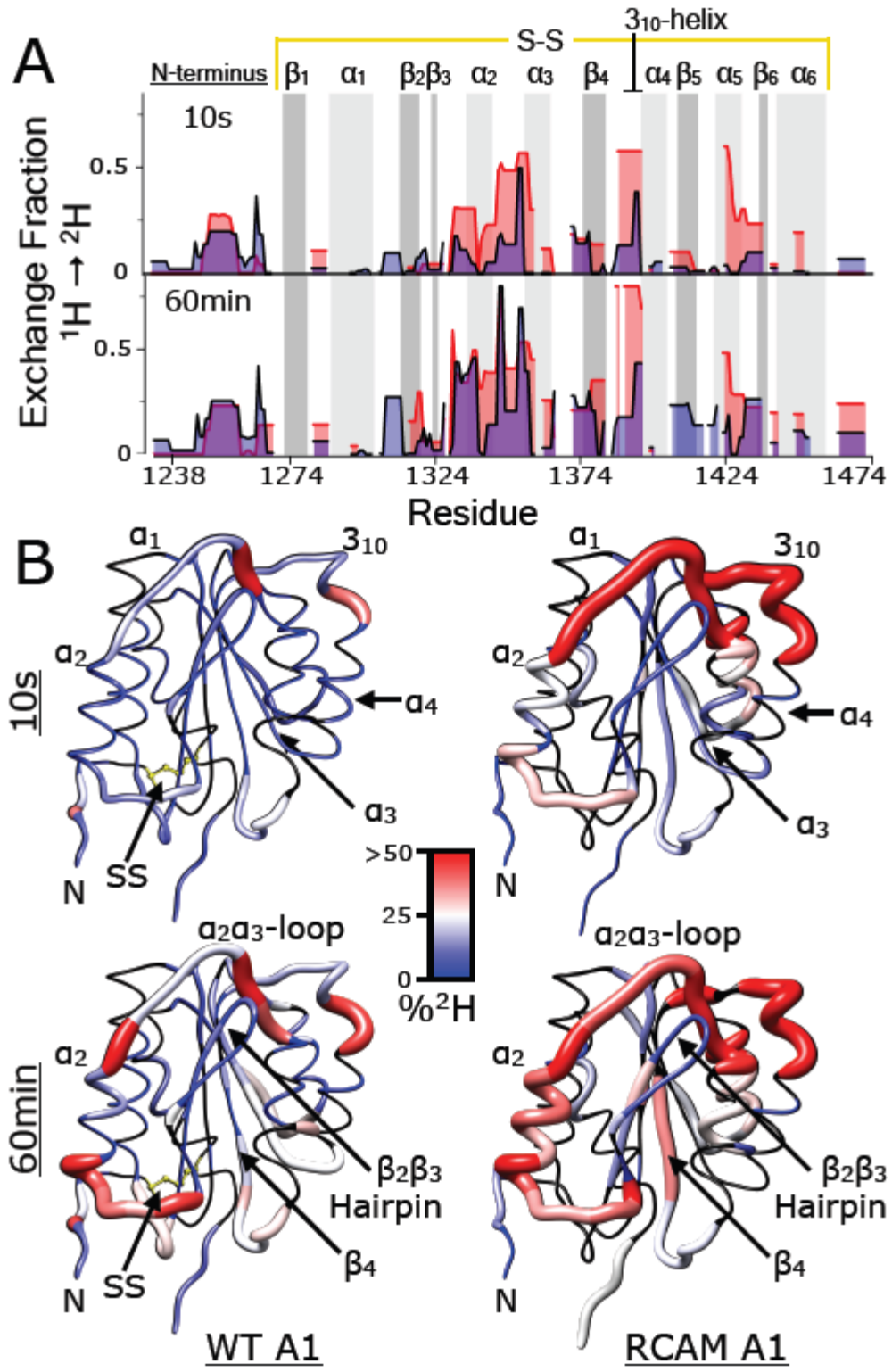

Figure 6

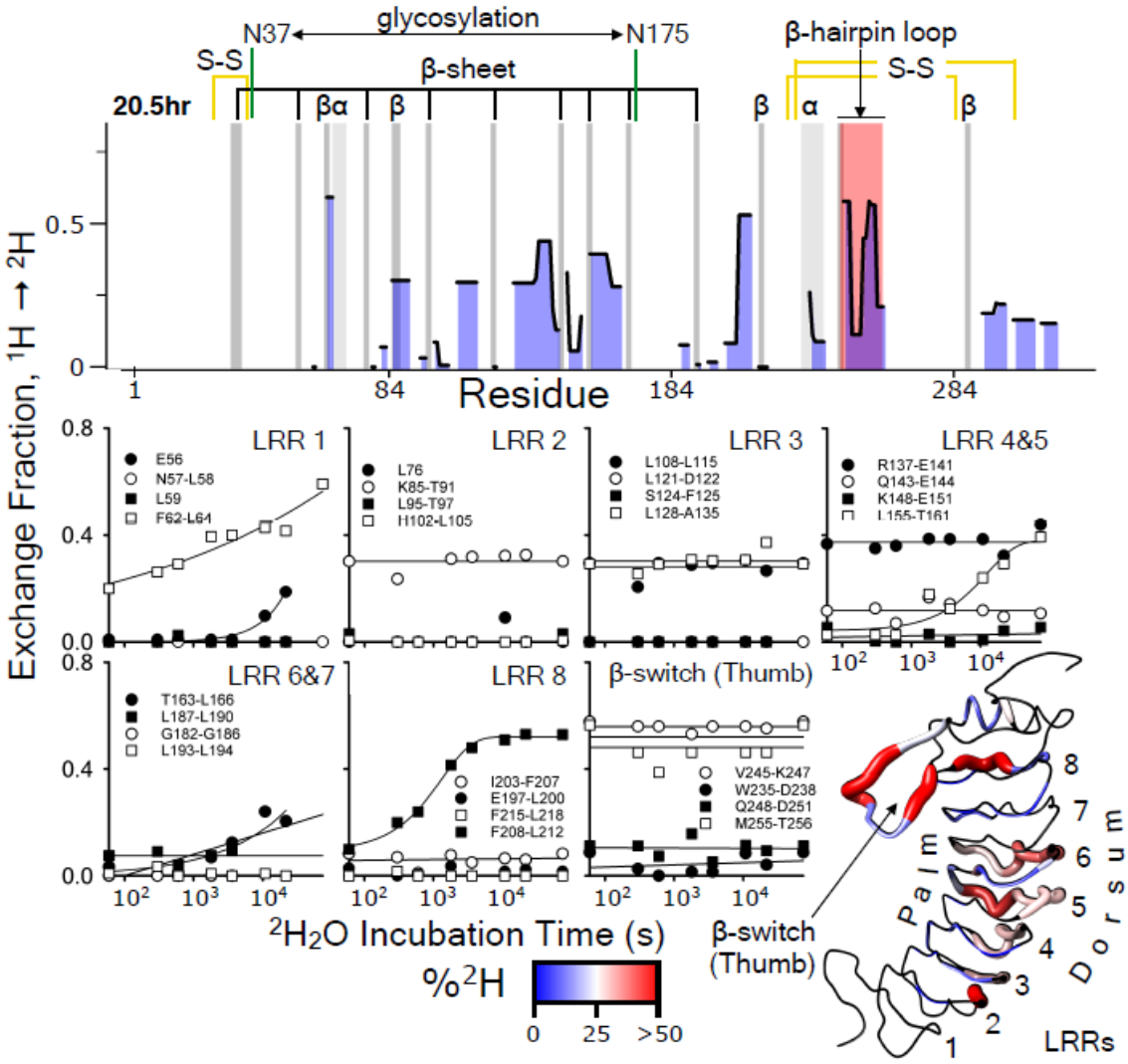

Figure 7

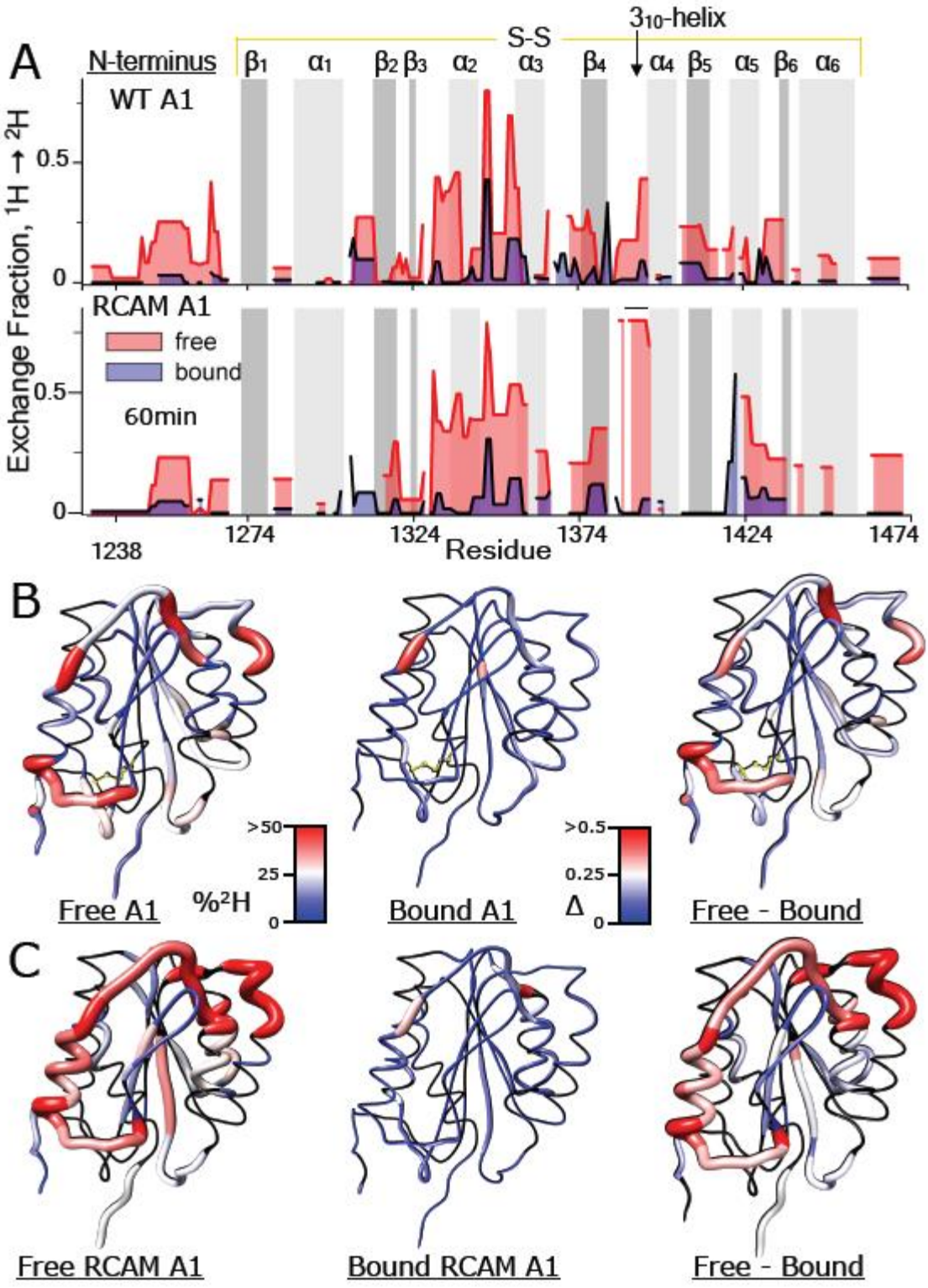

Figure 8

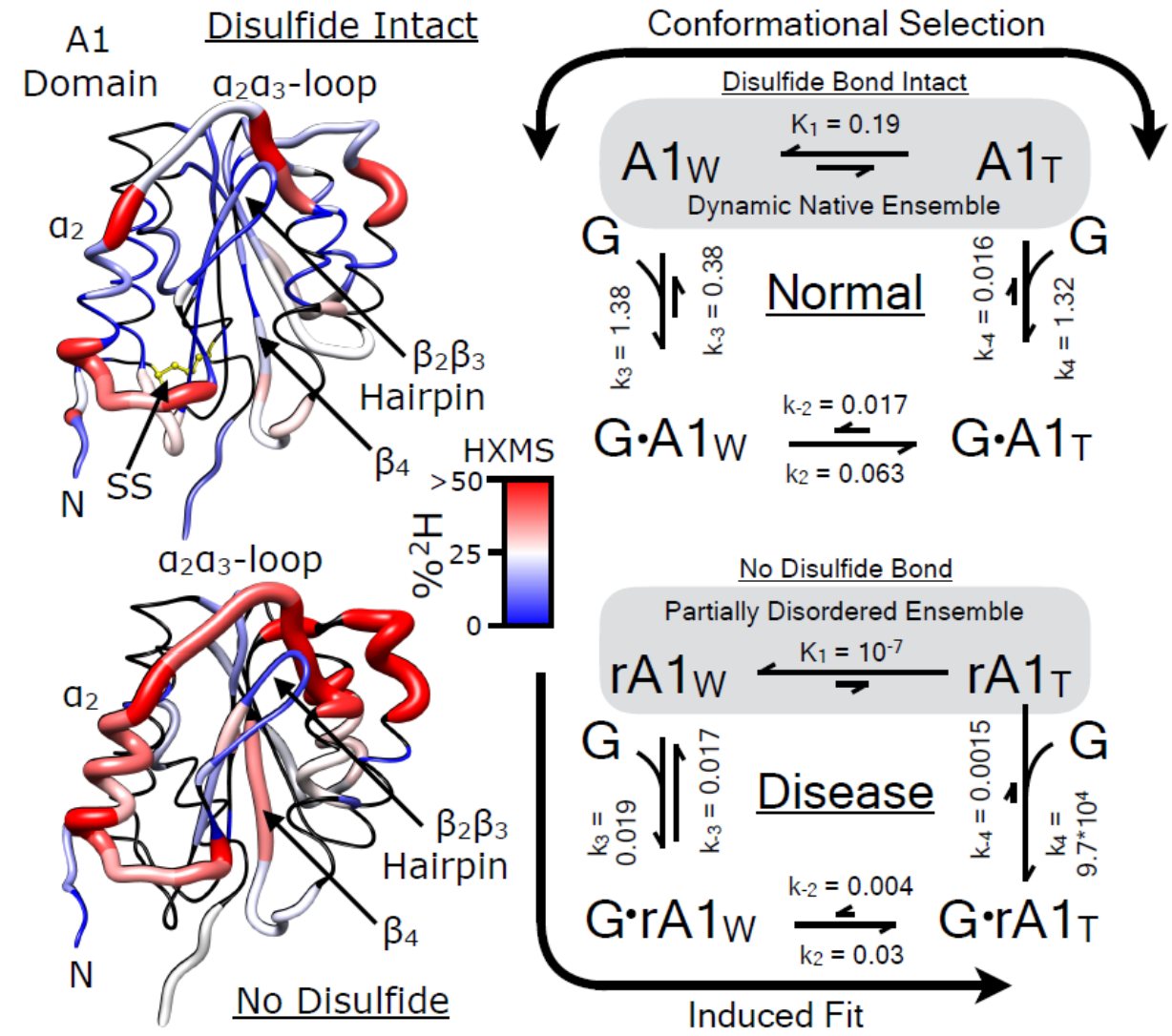

Graphical abstract

Research Highlights:

1. Normal platelet adhesion to VWF is driven by conformational selection between weak and and tight binding states of the platelet GPIbα binding A1 domain.
2. Mutation of the VWF A1 domain disulfide bond induces a gain-of-function type 2B VWD phenotype revealed by platelet clumping and DDAVP-induced transient thrombocytopenia in two VWD patients.
3. Loss of the disulfide enhances local disorder in A1, as observed by HXMS, that perpetuates abnormal high-affinity induced-fit binding of A1 to platelet GPIbα causing quantitatively deficient plasma VWF.